β

AIAA 80-1347R
Numerical Simulation of Three-Dimensional Boattail Afterbody Flowfields
G. S. Deiwert

Numerical Simulation of Three-Dimensional Boattail Afterbody Flowfields

G. S. Deiwert*

NASA Ames Research Center, Moffett Field, Calif.

The thin shear-layer approximations of the three-dimensional, compressible Navier-Stokes equations are solved for subsonic, transonic, and supersonic flow over axisymmetric boattail bodies at moderate angles of attack. The plume is simulated by a solid body configuration identical to those used in experimental tests. An implicit algorithm of second-order accuracy is used to solve the equations on the ILLIAC IV computer. The turbulence is expressed by an algebraic model applicable to three-dimensional flowfields with moderate separation. The formulation used is attractive in its independence of boundary-layer parameters. Such a simple model, however, is incapable of supporting detailed quantitative descriptions of complex shear flows. Nevertheless, good qualitative comparisons are found with three different sets of experimental data. Quantitative improvement will depend on improved turbulence transport descriptions.

Introduction

AFTERBODY flowfields are an important consideration in both aircraft and missile design. Considerable test efforts have been undertaken to enhance our understanding of this complex area (see, for example, Ref. 1). More recently, with our increasing computational ability, there has been considerable effort to numerically simulate such flows. The most challenging features for numerical simulation include the viscous-inviscid interaction in the external flow and the viscous-viscous interaction between the external flow and the exhaust jet. Basically, two different approaches have been considered to describe these flows: one is the patching technique whereby each region of the flowfield is analyzed separately and then patched together in some sort of iterative fashion to describe the entire flowfield and the other is the direct approach whereby the entire flowfield is described by a suitable subset of the Navier-Stokes equations. The primary advantage of the patching methods is their computational efficiency. The advantage of the Navier-Stokes methods is their natural treatment of the interaction between the different flow regimes.

Numerical studies made to date have been essentially confined to axisymmetric flows. When even the slightest flow angularity occurs, the problem becomes fully three dimensional and the interactions between the different flow regimes assume an even more complex character. In the real-world application of aircraft and missile systems, the afterbody configurations always experience three-dimensional flow. It is difficult to envision extension of the patching methods to describe these three-dimensional flowfields, leaving as the only feasible recourse, the Navier-Stokes methods. A capability to study the influence of a third-dimensional effect should contribute significantly to our understanding of afterbody flowfields.

It is the purpose of this paper to describe an approach for simulating afterbody flowfields for axisymmetric configurations at moderate angles of incidence and to compare typical results with experimental data. In this first report of such a study, the geometries will be confined to bodies of revolution with solid plume simulators. Comparisons with experiment are made for the subsonic, transonic, and supersonic flight regimes. All flowfields were assumed to be

fully turbulent. No attempt was made to test various turbulent transport models. Future efforts should address this issue as well as the consideration of real exhaust plumes.

Method

As a starting point the computer program described by Pulliam and Lomax[2] is used and extended to treat boattail configurations. This code is written for the ILLIAC IV computer and uses an implicit algorithm to solve the three-dimensional thin-shear-layer approximation to the Reynolds-averaged Navier-Stokes equations.

The numerical algorithm used is the fully implicit method described by Beam and Warming.[3] Approximate factorization of the algorithm operators makes this method particularly suitable to array processors such as the ILLIAC IV. This method was first used by Steger[4] to study two-dimensional flows; it was extended to three dimensions by Pulliam and Steger.[5] A detailed description of the equation set, notation, and boundary conditions is presented in Ref. 5. The particular code used in the present study treats the boundary conditions to a first-order error in time. Fourth-order dissipation terms are added explicitly and first-order temporal, second-order spatial dissipation terms are added implicitly.

For subsonic and transonic flows the solutions are generated in a timewise manner; the flow is accelerated from at-rest conditions to the desired freestream values. The timewise solution is continued until a steady state is realized. For supersonic flows the same procedure can be followed, but it is more efficient to generate a solution over the forebody using a parabolized Navier-Stokes code and approximate a starting solution over the afterbody based on the forebody solution. The forebody flowfield can then be used as a boundary condition and the thin-shear-layer Navier-Stokes solution advanced in time to a steady state in the afterbody region only. This is the procedure adopted in the present study. The parabolized Navier-Stokes solutions are obtained using the conical flow and marching codes of Schiff and Steger.[6]

Computational grids are constructed in a body-oriented sense so that radial grid lines on the forebody join the surface orthogonally, and on the afterbody are normal to the body axis. Streamwise grid lines are constructed between the body surface and a hemisphere cylinder outer boundary that is several diameters (typically 20) from the body axis. The streamwise grid lines are distributed radially in a geometric progression such that the first grid line off the body surface lies within the sublayer of the turbulent boundary layer. The
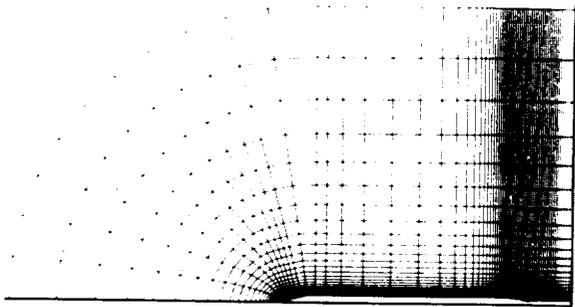
Fig. 1 Computational grid for Reubush configuration 2 boattail model.

Fig. 2 Comparison of surface pressure distributions over Reubush afterbody, configuration 2: $M_\infty = 0.4$, $Re_{d_m} = 1.5 \times 10^6$, $\alpha = 0$ deg.

third dimension is generated by rotating the two-dimensional grid about the cylindrical axis, maintaining a uniform angular separation between the rotated planes. A typical example of the computational grid is shown in Fig. 1. Grid stretching and clustering is used to focus resolution over the afterbody region.

Imposed boundary conditions include uniform freestream at the upstream and far field lateral boundaries, extrapolation at the downstream boundary, no slip and adiabatic wall on the body surface, and zero normal pressure gradient at the body surface. Solutions are initiated by gradually accelerating the body into a stationary field until the desired freestream speed is reached. This is done in the first 30 iterative passes. The solution is then continually advanced in time until a steady state is realized.

For supersonic flow computations a subset of the complete grid is used, beginning just ahead of the afterbody and extending to the downstream and outer boundaries. The upstream boundary condition is determined from a parabolized Navier-Stokes code[6] and the initial flowfield over the afterbody and solid plume simulator is approximated by the upstream boundary values. Planar symmetry is imposed across the plane passing through the windward and leeward generators. Typical grids used in the present study are $80 \times 48 \times 15$ for zero angle-of-attack cases and $80 \times 48 \times 39$ for nonzero angle-of-attack cases. Because two boundary points are necessary at the circumferential boundaries—one at the windward ray and one at the leeward ray—39 circumferential points on the half-body correspond to grid planes every 5 deg.

The turbulence transport model used in the present study is the two-layer algebraic eddy viscosity model suggested by Baldwin and Lomax.[7] In the inner layer the length scale is proportional to the distance away from the wall times the van Driest damping term, and the velocity scale is proportional to the length scale times the magnitude of the local vorticity. In the outer layer the velocity and length scales are functions of the local maxima of vorticity and are constant across the layer.

Computed Flows

Computations have been made for four boattail-plume simulator configurations and a variety of run conditions. Reubush[8] tested a series of eight circular arc afterbodies with both cylindrical plume simulators and real jet exhaust plumes for Mach numbers from 0.4 to 1.3 to determine the effectiveness of utilizing solid circular cylinders to simulate jet exhaust plumes. Reubush's "configuration 2" is simulated in the present study for freestream Mach numbers of 0.4 and 1.3 at zero angle of incidence. Benek[9] tested two different configurations, both with solid plume simulators, for Mach numbers ranging from 0.6 to 1.3, with the specific intent of providing data to validate predictive codes. Both of Benek's configurations are simulated in the present study for a freestream Mach number of 0.64 at zero angle of incidence. Shrewsbury[10] tested eight different afterbody configurations with cylindrical plume simulators for Mach numbers ranging from 0.56 to 1.0 and angles of incidence ranging from 0 to 8 deg. One Shrewsbury configuration is simulated in the present
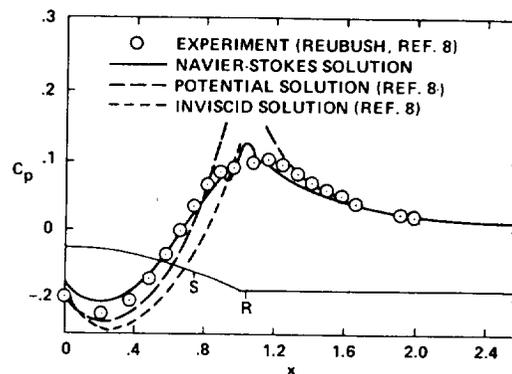
study for a freestream Mach number of 0.9 and angles of incidence of 0, 2, 4, and 6 deg.

All computations were performed using the full three-dimensional code. Only the Shrewsbury cases, however, are fully three-dimensional flows. All subsonic and transonic flow cases are computed using a blunted cone-cylinder boattail-solid plume simulator configuration. Experimentally the configurations all had pointed conical noses. Computationally, however, it is more efficient to treat blunted noses and avoid "stiffness" incurred by trying to wrap the computational grid around a sharp nose. Tests with the Reubush configuration and Benek configurations, whereby both sharp and blunted noses were considered, indicate no discernible difference in the flowfield in the vicinity of the boattail. For supersonic flows it is advantageous to consider only sharp conical noses and to use the parabolized Navier-Stokes codes on the forebody.

In all of the following results x is the axial position as measured from the forebody-afterbody junction and normalized by the forebody diameter d_m.

The first case considered is configuration 2 of Reubush[8] at a Mach number of 0.4 and zero angle of incidence. Here the entire flowfield is subsonic and the complexity of interaction between shocks and boundary layers and transonic flow effects are noticeably absent. Shown in Fig. 2 is a comparison of experimental and computed surface pressure distributions over the afterbody and plume simulator. The experimental data of Reubush are shown by the symbols and the present computation by the solid line. For comparison, a potential flow solution by the method of Hess and Smith[11] and an inviscid solution by the method of Keith et al.[12] are shown by dashed and dotted lines, respectively. These two solutions are taken directly from Ref. 8. The Hess and Smith result includes the effect of boundary-layer displacement thickness as incorporated by Reubush. The computational streamwise spacing over the afterbody was uniform at $\Delta x = 1/16$. Computations were also performed with an axisymmetric version of the Navier-Stokes code on a CDC 7600, using the same streamwise and radial grid and with a grid having twice the streamwise resolution over the afterbody. The differences between the solutions are slight, with the higher resolution axisymmetric solution showing the closest agreement with the experimental data.

The computation predicts separation at $x \approx 0.75$ and reattachment at $x \approx 1.05$; these are indicated by the points S and R, respectively, in the figure. The reattachment point corresponds to the point of maximum computed pressure. The experimental pressure maximum appears to be further downstream.

In a qualitative sense the present results look good and represent an improvement over the corresponding inviscid results. Quantitatively, however, the details of the solution near the boattail-plume junction may be open to question. The uncertainty in this region may be attributable as much to
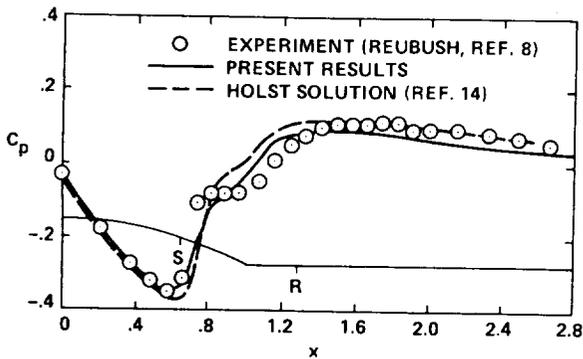
Fig. 3 Comparison of surface pressure distributions over Reubush afterbody, configuration 2: $M_\infty = 1.3$, $Re_{d_m} = 1.5 \times 10^6$, $\alpha = 0$ deg.
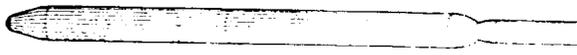

Fig. 4 AEDC boattail model, separated-flow configuration.

a lack of resolution as to oversimplified modeling of the Reynolds stresses. Additional observations are made concerning this question in subsequent comparisons with other experiments.

The second case considered is also Reubush configuration 2 at zero angle of incidence, but at a supersonic Mach number of 1.3. Shown in Fig. 3 is a comparison of computed and experimental surface pressure distributions over the afterbody and plume simulator. The present results are shown by the solid line, and a solution from Holst[13,14] is shown by the dashed line. Holst used an algebraic turbulence model in conjunction with his explicit Navier-Stokes code. He incorporated a relaxation formula in his eddy viscosity model to account for the nonequilibrium effects of the separated flow. The optimum relaxation parameter suggested in Ref. 13 was used to obtain the solution shown here.[14]

Both solutions do a poor job of describing the pressure plateau over the separated flow region. Both predict a separated flow region of comparable length, although the Holst solution indicates a downstream shift in the position of $\Delta x \approx 0.07$ compared with the present solution, which shows separation occurring at $x = 0.68$ and reattachment at $x \approx 1.31$. The present results show excellent agreement with experiment up to the predicted separation point. The Holst solution shows a delay in the onset of pressure recovery corresponding to the downstream shift in separation onset. Holst's study[13] indicated a strong dependence of the solution on turbulence modeling downstream of the separation point. This effect is probably most pronounced when large regions of separated flow, such as in the present case, are present. This suggests a need for more sophisticated turbulence models when there are large regions of flow reversal. As was observed for the $M_\infty = 0.4$ results the solution for $M_\infty = 1.3$ shows good qualitative agreement with experiment, but poor quantitative agreement over the boattail-plume junction.

Two solutions were obtained: one using the same ($80 \times 48 \times 15$) grid used for the $M_\infty = 0.4$ case and one using an abbreviated grid with the same resolution over the afterbody, but with upstream boundary conditions determined from the parabolized Navier-Stokes code of Schiff and Steger.[6] When the upstream boundary in the latter case is not positioned within the region of influence of the afterbody, the two solutions are the same. This affords the primary advantage of being able to increase the resolution over the afterbody for supersonic flows compared with subsonic and transonic flows when the maximum number of streamwise mesh points is limited.

Benek[9] performed a series of tests on two separate configurations—one designed for no separation and one to produce substantial separation—for the purpose of providing
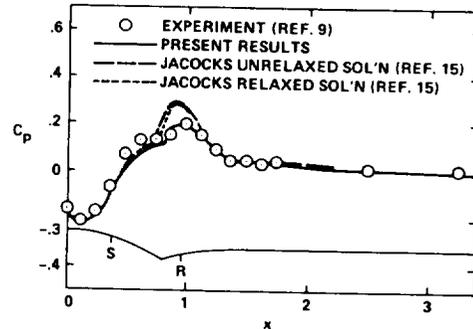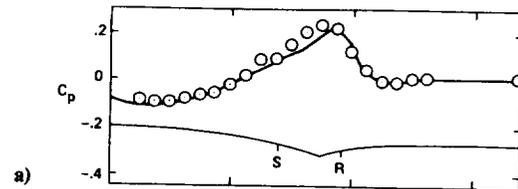

a)

b)

Fig. 5 Comparison of surface pressure distribution over AEDC afterbodies, $M_\infty = 0.64$, $Re_{d_m} = 2.886 \times 10^6$, $\alpha = 0$ deg: a) attached-flow configuration; b) separated-flow configuration.
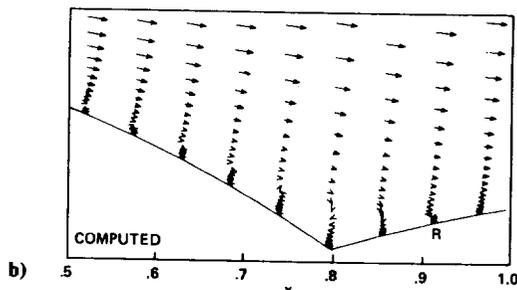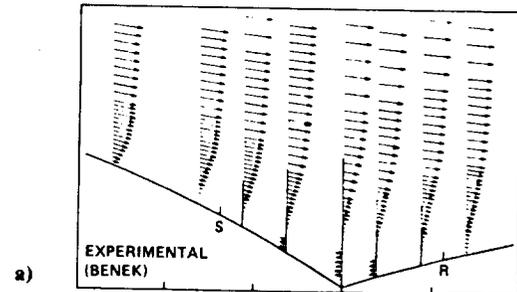

a)

b)

Fig. 6 Velocity distribution over AEDC separated-flow afterbody configuration, $M_\infty = 0.64$, $Re_{d_m} = 2.886 \times 10^6$, $\alpha = 0$ deg: a) experimental distribution (Benek[9]); b) computed distribution.
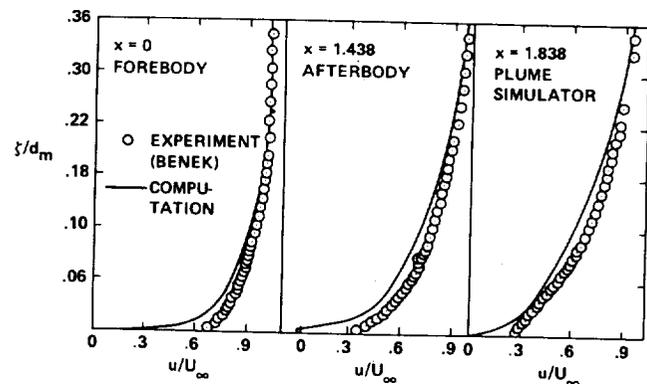

Fig. 7 Comparison of computed and measured velocity profiles over AEDC attached-flow afterbody configuration, $M_\infty = 0.64$, $Re_{d_m} = 2.886 \times 10^6$, $\alpha = 0$ deg.
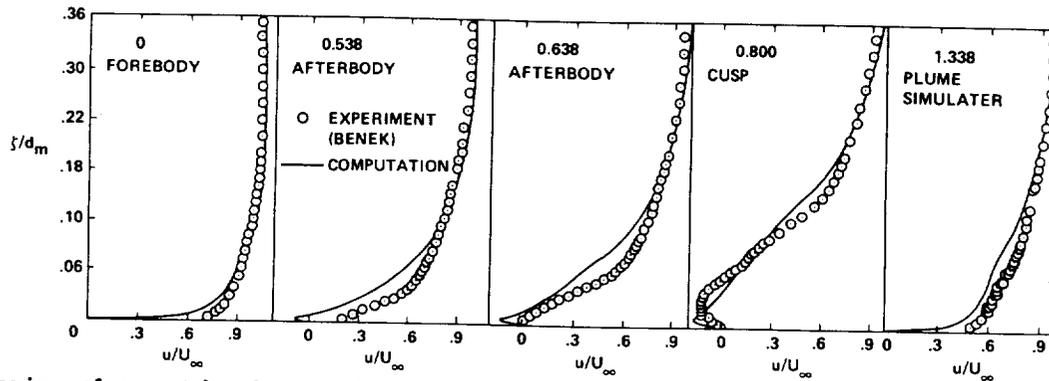
Fig. 8 Comparison of computed and measured velocity profiles over AEDC separated-flow afterbody configuration, $M_\infty = 0.64$, $Re_{d_m} = 2.886 \times 10^6$, $\alpha = 0$ deg.
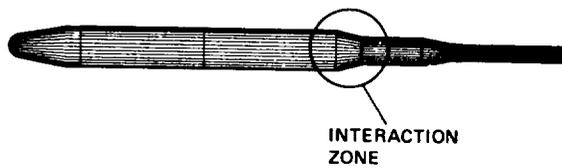

Fig. 9 Shrewsbury boattail model: $M_\infty = 0.9$, $Re_{d_m} = 2.9 \times 10^6$, $0 \le \alpha \le 6$ deg.
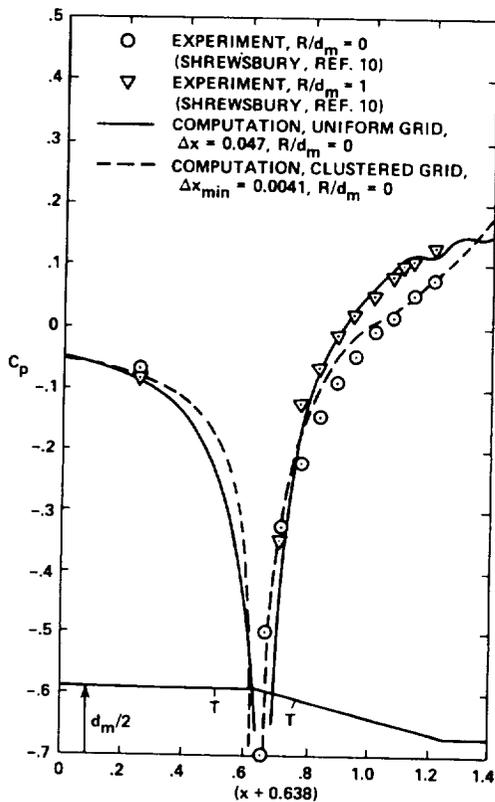

Fig. 10 Influence of forebody-afterbody juncture and grid distribution on afterbody pressure distribution, Shrewsbury configuration: $M_\infty = 0.9$, $Re_{d_m} = 2.9 \times 10^6$, $\alpha = 0$ deg.
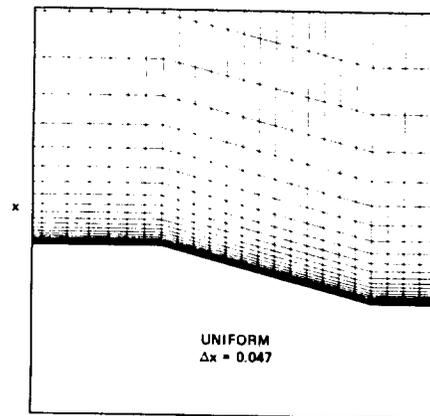

Fig. 11 Uniform grid over Shrewsbury afterbody, $\Delta x = 0.047$.

and both unrelaxed and relaxed algebraic eddy viscosity models, respectively. The unrelaxed model is identical to that used in the present study. Both Jacocks' unrelaxed model result and the present result are identical up to the boattail-plume junction. The pressure distribution on the solid plume, however, seems better predicted by the present code. Neither solution performs well in predicting the pressure plateau on the afterbody. The effect of including relaxation is indicated by Jacocks' second solution. Significant improvement is not realized. This result and the solution by Holst for the Mach 1.3 case of Reubush strongly suggest that relaxation is not the panacea for all afterbody flow simulations.

The solutions for both geometries were generated using a uniform streamwise grid over the afterbody and near-plume surface. Fifteen points describe the afterbodies with $\Delta x = 0.118$ for the attached flow case and $\Delta x = 0.053$ for the separated case. A very thin reverse-flow region is predicted for the attached-flow configuration extending from $x \approx 1.38$ to 1.89. Such flow reversal was not observed experimentally in surface flow visualizations using tufts when the freestream Mach number was 0.80. For the separated-flow configuration, separation is predicted at $x \approx 0.32$ and reattachment at $x \approx 0.91$. This corresponds to experimental values of separation at $x \approx 0.66$ and reattachment at $x \approx 0.91$. Comparison of the computed velocity profiles and experimental profiles measured using a laser velocimeter are shown in Fig. 6 for the boattail-plume junction region of the separated-flow configuration. There is remarkable agreement in the thickness and reattachment location of the two reverse flowfields. The computation, however, predicts a thin reverse-flow region extending quite a bit farther upstream than the experimental results. These two solutions indicate that the computation is more prone to producing separated flows in adverse pressure gradient regions.

Three velocity profile comparisons for the attached flow configuration are shown in Fig. 7. The profile at $x = 0$ is just at the beginning of the afterbody, the profile at $x = 1.438$ is on

a data base for testing computer codes. The separated flow configuration simulated in the present study is shown in Fig. 4. The attached flow configuration is similar, but with a more gradual afterbody variation. Presented in Fig. 5 is a comparison between computed and measured surface pressure distributions at $M_\infty = 0.64$ for both the attached flow configuration (Fig. 5a) and the separated flow configuration (Fig. 5b). Present results are indicated by the solid line. In Fig. 5b the dashed and the dotted lines are solutions obtained by Jacocks[15] using a mixed explicit-implicit Navier-Stokes code
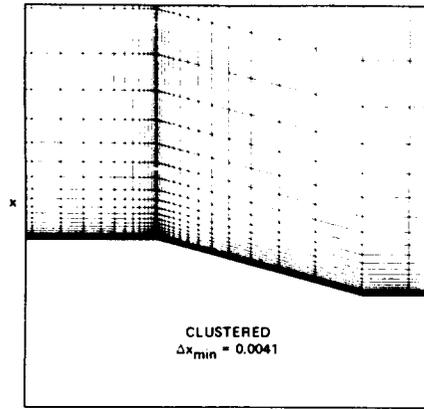
Fig. 12   Clustered grid over Shrewsbury afterbody, $\Delta x_{min} = 0.0041$.

the afterbody, and the profile at $x = 1.838$ is on the plume simulator. The profile comparison at $x = 0$ shows a computed profile that is not as fully developed as the experimental profile. This in itself will lead to greater susceptibility to separation in adverse pressure gradient regions. There is sufficient resolution in the computational grid to define the profile shape, and the afterbody is positioned far enough downstream from the nose so that the flow ahead of the boattail should correspond to fully developed axisymmetric flow along an infinite cylinder. Hence, the disparity is probably due to viscosity—empirical or artificial or both. The two profile comparisons farther downstream also exhibit the same trend, that is, that the computed profiles are not as fully developed as the experimental profiles. The computed profile on the afterbody at $x = 1.438$ shows a small reversal.

Five velocity profile comparisons for the separated flow model are shown in Fig. 8. The profile at $x = 0$ is just at the beginning of the afterbody, the profiles at $x = 0.538$ and 0.638 are on the afterbody, the profile at $x = 0.800$ is at the afterbody-plume junction, and the profile at $x = 1.338$ is on the plume simulator. The same lack of fullness in the computed profiles observed previously for the attached-flow model results is evident here. In addition, a detailed comparison in the reverse-flow region is possible, especially at $x = 0.800$. Here the qualitative comparison is reasonable, but detailed differences suggest viscosity problems again.

Surface pressure and velocity profile comparisons with experiment for the two Benek cases show that the trends of flowfield response to the afterbody are reasonably well predicted. Lack of precise agreement in some of the details points to problems in the modeling of the eddy viscosity and perhaps with the artificial viscosity. From the length scales obvious in these two flows the thin-layer approximation does not appear to be violated.

Shrewsbury[10] studied the effect of boattail juncture shape on afterbody drag. Of particular interest for the present study is the series of measurements made on a 15 deg conical afterbody at the transonic Mach number of 0.9 for angles of incidence of 0, 2, 4, and 6 deg. These provide the basis of comparison for the three-dimensional computations for afterbodies with plume simulators.

The configuration simulated is shown in Fig. 9. It is composed of a blunted cone-cylinder forebody followed by a 15 deg conical afterbody with a sharp junction and a cylindrical plume simulator, which is mounted on a smaller diameter cylindrical sting. The region of computational and experimental interest is circled in the figure.

In Fig. 10 is a comparison of computed and experimental surface pressures over the afterbody for axisymmetric flow (angle of incidence of 0 deg). The solid line corresponds to computed results using a uniform grid over the afterbody with a spacing of $\Delta x = 0.047$. This grid, which is illustrated in Fig. 11, contains 14 points to describe the afterbody. The uniform grid solution compares well with the experimental results
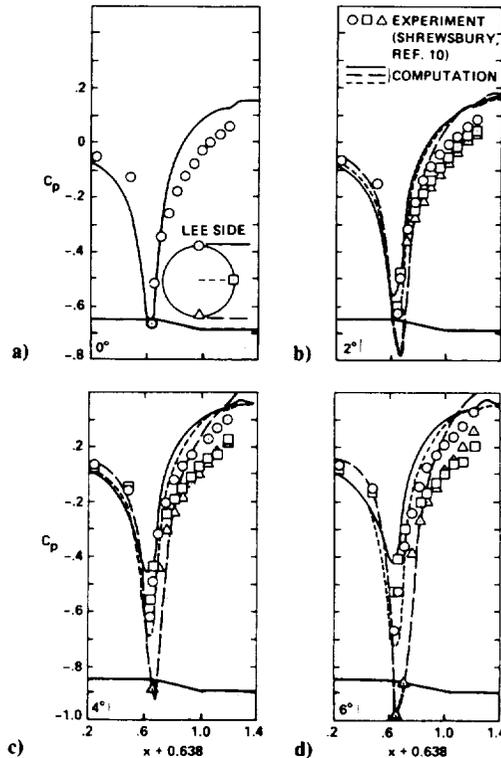

Fig. 13   Comparison of surface pressure distributions over Shrewsbury afterbody, $M_\infty = 0.9$, $Re_{d_m} = 2.9 \times 10^6$, $R/d_m = 0$: a) $\alpha = 0$ deg; b) $\alpha = 2$ deg; c) $\alpha = 4$ deg; and d) $\alpha = 6$ deg.

shown by the solid triangles. These experimental results, however, correspond to a conical boattail having a rounded juncture, with a radius of curvature of $R/d_m = 1.0$, between the forebody and afterbody. Shrewsbury also performed the experiment with a sharp juncture. Both the rounded juncture and sharp juncture configurations are shown in Fig. 10 where the T's denote the tangency points of the rounded junction. The difference between the two configurations is not visually discernible in the figure. The open circle symbols correspond to experimental results for the sharp junction configuration and show slower pressure recovery on the afterbody. The effect of the forebody-afterbody junction is significant. In an attempt to resolve the sharp junction computationally, a clustered grid (Fig. 12) was used where the minimum mesh spacing, occurring at the junction, is $\Delta x_{min} = 0.0041$, more than one order smaller than the uniform grid spacing. Again, 14 points are used to define the afterbody. The computed pressures using this clustered grid are shown by the dashed line in Fig. 10. The improvement is significant and results compare favorably with the experimental results for the sharp-junction configuration.

A series of computations was made for angles of incidence of 0, 2, 4, and 6 deg, using the uniform grid shown in Fig. 11. For nonzero angles of incidence a circumferential spacing of 5 deg is used; for axisymmetric flow a spacing of 15 deg is used. Surface pressure for these cases are compared with experiment in Figs. 13a-d. Figure 13a is for zero angle of incidence and is a repeat of the open circles and solid-line solution shown in Fig. 10. Figures 13b-d are for angles of incidence of 2, 4, and 6 deg, respectively. The experimental data are shown by the symbols: the circles, squares, and triangles correspond to the leeward, lateral, and windward rays, respectively. The corresponding computed results are shown by solid, dotted, and dashed lines. The rounding effect of the uniform grid is evident in all figures. On the other hand, the levels and trends are quite well predicted by the computations. In fact, if a "correction" was approximated from Fig. 13a and applied to all the computed results in Figs. 13b-d the comparisons would look quite good. The conclusion
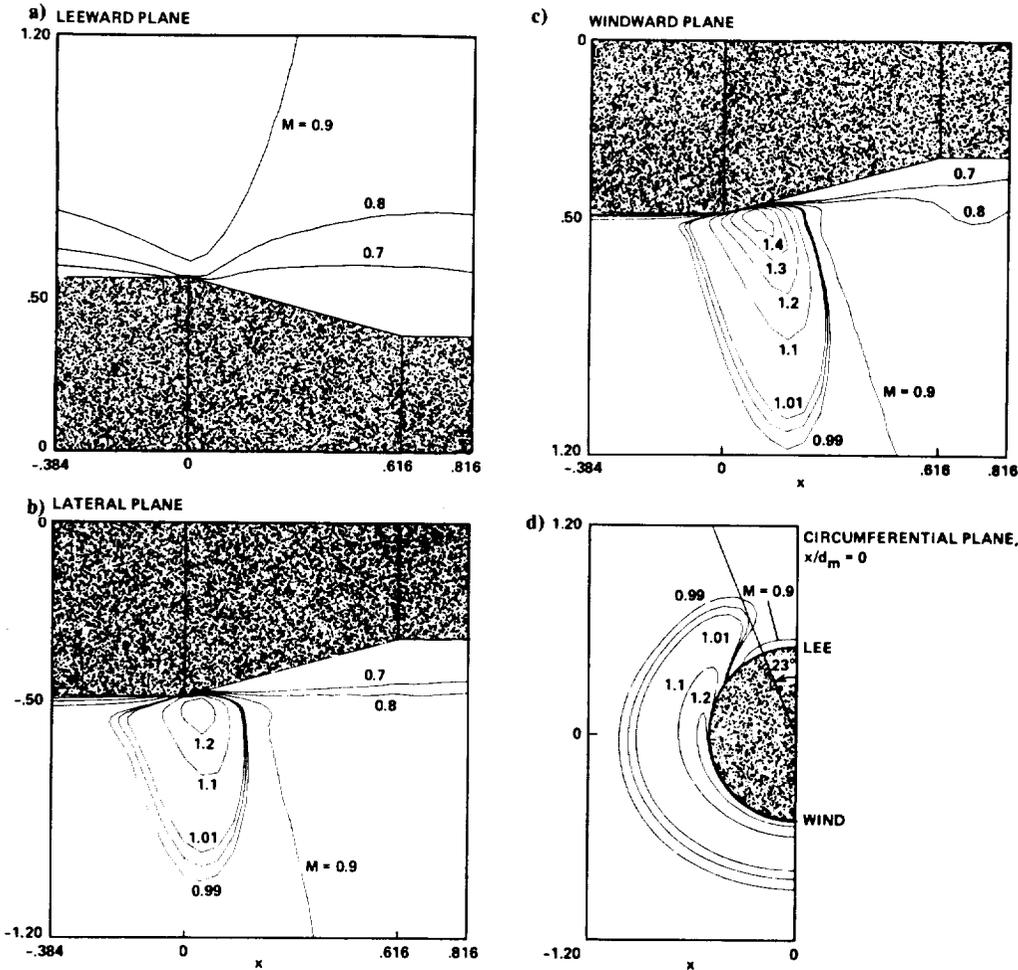
Fig. 14   Computed Mach contours over Shrewsbury afterbody, $M_\infty = 0.9$, $Re_{d_m} = 2.9 \times 10^6$, $\alpha = 6$ deg: a) leeward plane; b) lateral plane; c) windward plane; and d) circumferential plane, $x = 0$.
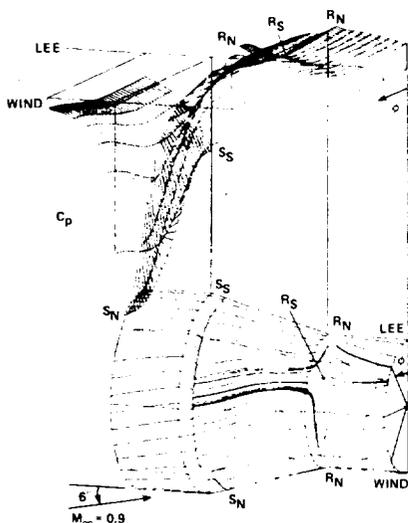

Fig. 15   Surface flow pattern and pressure map for Shrewsbury afterbody, $M_\infty = 0.9$, $Re_{d_m} = 2.9 \times 10^6$, $\alpha = 6$ deg.
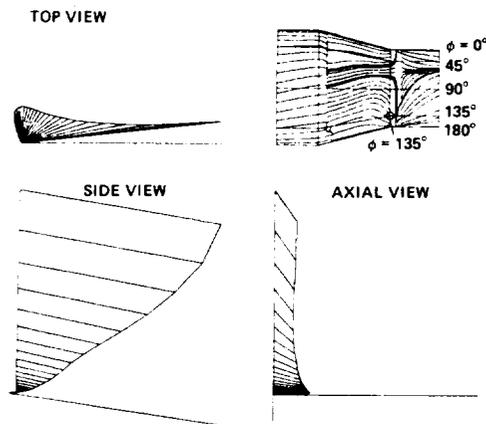

Fig. 16   Skewed velocity profile on Shrewsbury afterbody at $x = 0.616$, $\phi = 135$ deg, $M_\infty = 0.9$, $Re_{d_m} = 2.9 \times 10^6$, $\alpha = 6$ deg.

is that the three-dimensional effects are fairly well handled by the code.

Shown in Fig. 14 are computed Mach contours for the leeward, lateral, windward, and circumferential planes for the 6 deg solution. The flow is entirely subsonic on the leeward side to within ±23 deg from the leeward generator. It is transonic in the lateral and windward planes, with shocks

impinging the boundary layer downstream of the forebody-boattail junction at $\Delta x \simeq 0.17$ and 0.23, respectively. A cross section of the Mach contour pattern at $x = 0$ is shown in Fig. 14d. The sonic line is oblated between the windward and lateral planes at a radius nearly equal to the body diameter. Between the lateral and leeward planes the flow becomes subsonic and the sonic line closes in the boundary layer.

A perspective view of the computed surface pressure map and corresponding surface shear flow pattern over the afterbody for the 6 deg angle-of-incidence case is shown in Fig. 15. The back plane of the pressure map corresponds to the

leeward generator. The outward coordinate is rotation angle varying from zero to π from the leeward to the windward generator, drawn along the zero pressure coefficient plane. Reference lines are drawn corresponding to forebody-afterbody junction and afterbody-plume simulator junction. Beneath the pressure map is the surface shear pattern, which closely approximates an oil-flow pattern. Flow is in the streamwise direction on the forebody with cross flow from the windward to the leeward side. The cross flow is greatest on the lateral side of the body, corresponding to the favorable cross-flow pressure gradient in the same direction evident on the upstream end of the pressure map. Just after the forebody-afterbody junction there is a line of separation extending completely around the afterbody and having a separation saddle point (S_S) on the leeward generator and a separation node (S_N) on the windward generator. This line of separation occurs upstream of the shock/boundary-layer interactions and downstream of the line of minimum pressure connecting the leeward and windward generators. There is a pressure saddle point (S_S) on the leeward generator and a pressure node (S_N) (minimum) on the windward generator just upstream of the separation saddle point and node on the surface shear flow. Flow moves from the surface saddle point to the node.

The flow is reverse downstream of the line of separation over the rest of the afterbody up to the line of reattachment on the solid-plume simulator. The line of reattachment completely surrounds the body with nodes on both the leeward and windward generators (R_N) and a saddle point in between (R_S). The flow is from the nodes toward the saddle points. Corresponding to the reattachment nodes and saddles are nodes and saddles on the surface pressure map with the nodes occurring on the leeward and windward generators (R_N) and the saddle points in between (R_S). Downstream of the line of reattachment the flow is in the streamwise direction again. Two more nodes exist in the flowfield, one at the stagnation point near the nose of the forebody and one downstream at infinity; topological laws are satisfied.

Near the body surface, convective forces are negligible and shear forces are balanced by pressure forces. Hence, as we can see in Fig. 15, the surface shear pattern corresponds to the pressure gradient pattern of the surface pressure map quite well. It should be possible, given the surface pressure distribution and the existence of the singular points, to approximately reconstruct the surface shear pattern.

A final observation concerns skewness in the boundary layer, particularly over the afterbody where the secondary flow is significant. For most of the flowfield the boundary-layer profiles are essentially two dimensional. On the aft portion of the afterbody, on the windward side, skewness is quite evident. An example of the velocity profile is shown in Fig. 16 where three views can be seen: top, side, and streamwise. A question associated with the flow in this region is the validity of a scalar eddy-viscosity model to represent the shear-stress tensor and the sensitivity of the secondary flow to the Reynolds stresses. It is hoped that with increased computing power, more sophisticated turbulence models can be considered to address this question.

Concluding Remarks

The development of a method for simulating three-dimensional afterbody flowfields has been described. The thin-shear-layer Reynolds-averaged Navier-Stokes equations have been solved numerically, using an implicit algorithm, for a variety of afterbody flows of increasing complexity. Qualitatively, the results are excellent; quantitatively, there appear areas where further study is necessary. The areas of particular concern are empirical turbulence modeling, effects of artificial viscosity, and the influence of grid-point distribution. Nonetheless, the method in its present form appears powerful enough to perform complex preliminary analyses or parametric studies.

References

[1] Ferri, A., ed., "Improved Nozzle Testing Techniques in Transonic Flow," AGARD-AG-208, Oct. 1975.

[2] Pulliam, T. H. and Lomax, H., "Simulation of Three-Dimensional Compressible Viscous Flow on the Illiac IV Computer," AIAA Paper 79-206, New Orleans, La., Jan. 1979.

[3] Beam, R. and Warming, R. F., "An Implicit Finite-Difference Algorithm for Hyperbolic Systems in Conservation-Law-Form," Journal of Computational Physics, Vol. 22, Sept. 1976, pp. 87-110.

[4] Steger, J. L., "Implicit Finite-Difference Simulation of Flow About Two-Dimensional Geometries," AIAA Journal, Vol. 16, July 1978, pp. 679-686.

[5] Pulliam, T. H. and Steger, J. L., "On Implicit Finite Difference Simulations of Three-Dimensional Flow," AIAA Journal, Vol. 18, Feb. 1980, pp. 159-167.

[6] Schiff, L. B. and Steger, J. L., "Numerical Simulation of Steady Supersonic Viscous Flow," AIAA Paper 79-130, New Orleans, La., Jan. 1979.

[7] Baldwin, B. S. and Lomax, H., "Thin Layer Approximation and Algebraic Model for Separated Turbulent Flows," AIAA Paper 78-257, Huntsville, Ala., Jan. 1978.

[8] Reubush, D. E., "Experimental Study of the Effectiveness of Cylindrical Plume Simulators for Predicting Jet-on Boattail Drag at Mach Numbers up to 1.30," NASA TN D-7795, 1974.

[9] Benek, J. A., "Separated and Nonseparated Turbulent Flows about Axisymmetric Nozzle Afterbodies, Part I, Detailed Surface Measurement," AEDC-TR-78-49; "Part II, Detailed Flow Measurement," AEDC-TR-79-22, Oct. 1979.

[10] Shrewsbury, G. D., "Effect of Boattail Juncture Shape on Pressure Drag Coefficients of Isolated Afterbodies," NASA TM X-1517, 1968.

[11] Hess, J. L. and Smith, A. M. O., "Calculation of Potential Flow About Arbitrary Bodies," Progress in Aeronautical Sciences, Vol. 8, edited by D. Kuchemann, Pergamon Press, Ltd., 1967, pp. 1-138.

[12] Kieth, J. S., Ferguson, D. R., Merkle, C. L., Heck, P. H., and Lahti, D. J., "Analytical Method for Predicting the Pressure Distribution About a Nacelle at Transonic Speeds," NASA CR-2217, 1973.

[13] Holst, T. L., "Numerical Solution of Axisymmetric Boattail Fields with Plume Simulators," AIAA Paper 77-224, Los Angeles, Calif., Jan. 1977.

[14] Holst, T. L., NASA Ames Research Center, Moffett Field, Calif., private communication, 1980.

[15] Jacocks, J. L., "Computation of Axisymmetric Separated Nozzle—Afterbody Flow," AEDC-DR-79-71, Jan. 1980.